POLITECNICO DI TORINO
Repository ISTITUZIONALE

Convection in the subsurface ocean of icy moons and response of the upper ice layer

*Original*
Convection in the subsurface ocean of icy moons and response of the upper ice layer / Pagnoscin, S., Von Hardenberg, J., Brucato, J.R., Provenzale, A.. - In: ICARUS. - ISSN 0019-1035. - 446:(2026). [10.1016/j.icarus.2025.116875]

*Availability:*
This version is available at: 11583/3008848 since: 2026-03-17T00:22:19Z

*Publisher:*
Elsevier

*Published*
DOI:10.1016/j.icarus.2025.116875

*Terms of use:*

This article is made available under terms and conditions as specified in the corresponding bibliographic description in the repository

*Publisher copyright*

(Article begins on next page)

15 November 2026

Icarus 446 (2026) 116875

Contents lists available at ScienceDirect

Icarus

journal homepage: www.elsevier.com/locate/icarus

# Convection in the subsurface ocean of icy moons and response of the upper ice layer

Silvia Pagnoscin [a,b,c,*], Jost von Hardenberg [d], John Robert Brucato [b], Antonello Provenzale [c]

[a] Department of Physics and Astronomy, University of Florence, Via G. Sansone 1, Sesto Fiorentino, Firenze, Italy
[b] INAF - Astrophysical Observatory of Arcetri, Largo E. Fermi, 5, Firenze, Italy
[c] Institute of Geosciences and Earth Resources, CNR, Via Moruzzi 1, 56124 Pisa, Italy
[d] Department of Environment, Land, and Infrastructure Engineering, Politecnico di Torino, 10129 Torino, Italy

ARTICLE INFO

*Keywords:*
Planetary science
Galilean satellites
Hydrodynamical simulations
Astrobiology

ABSTRACT

The main reservoirs of liquid water in the Solar System are hidden beneath the icy shells of some of the "icy moons" orbiting the gas giants Jupiter and Saturn. Although these moons lie well outside the traditional habitable zone, tidal forces exerted by their parent planet and internal radiogenic heating can sustain subsurface oceans of liquid water. These environments may offer the necessary conditions for life, making icy moons key targets in the search for extraterrestrial biospheres. Unfortunately, direct exploration of these oceans remains out of reach by current space mission technology, which is limited to surface observations. However, surface activity observed on several of these moons suggests that internal processes may be coupled with surface dynamics, potentially enabling surface-subsurface interactions. Previous global models have shown that large-scale fluid motions within the oceans may lead to latitude-dependent variations in heat flux at the ice-ocean boundary. In this study, we investigate intermediate-scale, localized convective dynamics within the subsurface oceans of icy moons, showing that these oceans can be dominated by intense thermal convection which can generate differential heat fluxes and local interactions at the ice-water interface. To explore this issue, we numerically integrate a simplified turbulent convective fluid model, coupled with a linear approximation for the freeze-melt processes of the overtopping ice layer. We observe that the resulting spatial variability in basal melting and freezing rates could induce thickness variations of the ice shell. These predictions can be tested by upcoming missions such as ESA's JUpiter ICy moons Explorer through gravity and altimetry measurements, offering new insights into the physical coupling between surface and interior also at small spatial scales.

## 1. Introduction

Liquid water is one of the fundamental requirements for life as we know it, as essential biochemical reactions rely on water to assemble the building blocks of life. Water serves as the "universal solvent," enabling cells to transport and utilize substances such as oxygen and nutrients; and it contributes to maintaining cellular structure (Pohorille and Pratt, 2012). From this perspective, the search for life in the universe has always been closely linked to the search for liquid water (Irion, 2002). In this framework, the circumstellar habitable zone is defined as the region of a planetary system where liquid water can exist on the surface of a celestial body. However, the largest reservoirs of liquid water in the Solar System are not necessarily found within the habitable zone defined in this way but are hidden beneath the surfaces of several icy moons of the gas giants, namely Jupiter and Saturn (Nimmo and Pappalardo, 2016). In these environments, tidal heating generated by the gas giants, along with internal heating from radioactive decay in a silicate mantle, sustains subsurface liquid water oceans that may provide the necessary conditions for life to emerge and persist. Several studies investigated the potential habitability of these worlds (Vance et al., 2018) and the survivability of potential ecosystems (Chyba and Phillips, 2001; Weber et al., 2023). This makes icy moons a primary target for Solar System exploration when dealing with the search for extraterrestrial life.

These satellites are directly accessible to space missions and have already been explored in the past. NASA's Galileo mission investigated the icy moons of Jupiter, while NASA's Cassini mission studied the icy moons of Saturn. New missions entirely devoted to Jupiter's icy ocean worlds—Europa, Ganymede, and Callisto—are currently on their way.

* Corresponding author at: Department of Physics and Astronomy, University of Florence, Via G. Sansone 1, Sesto Fiorentino, Firenze, Italy.
*E-mail address:* silvia.pagnoscin@unifi.it (S. Pagnoscin).

https://doi.org/10.1016/j.icarus.2025.116875
Received 14 July 2025; Received in revised form 3 November 2025; Accepted 4 November 2025
Available online 6 November 2025
0019-1035/© 2025 The Authors. Published by Elsevier Inc. This is an open access article under the CC BY-NC-ND license (http://creativecommons.org/licenses/by-nc-nd/4.0/).

NASA's Europa Clipper will focus on Europa, one of the most promising candidates in the search for extraterrestrial life owing to the possible direct interactions between its subsurface ocean and the rocky mantle (Vance et al., 2023). This connection may support water-rock interactions and, consequently, potential hydrothermal systems, which can have played a crucial role also in the emergence of life on Earth, by providing prebiotic molecules and essential nutrients (Westall et al., 2018). Meanwhile, ESA's JUICE (JUpiter ICy moons Explorer) mission will primarily study Ganymede, the largest moon in the Solar System, which appears to host a subsurface ocean that could be the most extensive liquid water reservoir in the entire planetary system.

Today's technology allows access only to the surface, enabling the investigation of morphology and composition and providing indirect clues about the internal structure (Schubert et al., 2004). However, it does not permit direct exploration of the subsurface oceans, leaving them largely beyond our measurement capabilities. Nevertheless, these worlds appear to be active today (Becker et al., 2023; Rovira-Navarro et al., 2024)—or have been in the past (Lee Allison and Clifford, 1987)—potentially supporting connections between the ocean and the surface. If such connection areas, or "hotspots," are identified, surface observations could offer valuable insights into the characteristics of the hidden oceans, helping to determine whether they could sustain potential ecosystems. Finding hotspots depends on the dynamics of the internal oceans (Soderlund et al., 2014) that can transport heat from the bottom of the ocean to the water-ice interface, on the dynamics of the ice shell (Mitri and Showman, 2005; Soderlund, 2019) and on the effects of tidal stresses (Moore, 2000).

Previous studies on the dynamics of ice-covered oceans mostly addressed large-scale, planetary dynamics. Some studies focused on thermal effects, showing enhanced heat transport towards the equator; others emphasized the role of salinity and ice melting/freezing processes, highlighting the formation of Taylor columns and a more uniform latitudinal heat distribution. For instance, Soderlund et al., 2014 demonstrated that large-scale thermal convection can drive equatorward heat fluxes, while Ashkenazy and Tziperman (2021) showed that salinity-dominated stratification may lead to more symmetric circulation patterns and Terra-Nova et al. (2023) explored the effects of a non-homogeneous heat flux at the ocean bottom. In doing so, however, such studies had to necessarily discard a more detailed and spatially-resolved description of the smaller-scale turbulent convective motions possibly existing in the oceans and of the associated vertical heat transfer processes. Currently, it is not yet possible to formulate a numerical description of icy-moon oceans encompassing the whole range of scales from turbulent convective plumes to the global ocean circulation.

The present study provides a complementary view of the ocean dynamics, and it focuses on the role of the (expectedly turbulent) km-scale convective dynamics of the hidden oceans, with special attention on the vertical heat transfer mechanisms associated with this intermediate-scale turbulent convection. In this context the role of rotating convection is crucial since, as outlined in previous studies (Brummell et al., 1996; Julien and Knobloch, 1998; Currie et al., 2020), it reorganizes plumes into anisotropic structures and alters transport laws. From this perspective, this work intends to quantify the role of turbulent convective processes on water-ice interaction and thus on the generation of connection hotspots. The aim is to determine if and where the interface can undergo phase changes due to the upcoming heat flux generated by convection and quantifying it with a proper description. It leads to the definition of maximum heating and freezing at different latitudes, a quantification of the topographic profile of the water-ice interface and the suggestion of the typical dimensions of the hotspots.

To isolate the thermal contribution, a simplified yet fundamental fluid dynamics model was adopted, based on Rayleigh-Bénard (RB) convection. The system is composed of a fluid layer heated from below and cooled from above and is a cornerstone for studying buoyancy-driven turbulence (Goluskin, 2016). The model configuration adopted here describes a three-dimensional, rotating incompressible fluid layer bounded above and below by rigid horizontal surfaces and periodic lateral boundary conditions (Passoni et al., 2002; von Hardenberg et al., 2008; Novi et al., 2019). This setup is meant to simulate a local portion (with horizontal scale of a few hundred kilometers) of the ocean at various latitudes in a Cartesian geometry. The convective dynamics is complemented by modeling the freeze-melt processes of the overtopping ice layer, which allows to estimate ice thickness variations as a result of the convective motions in the ocean. This phenomenon has been previously investigated with complex and fully coupled models (Rabbanipour Esfahani et al., 2018; Yang et al., 2023). Here, we adopted a simplified, linear approximation for the freeze-melt processes consistent with our formulation, which keeps the problem tractable.

Even though the conceptual fluid model used here is extremely simplified, the results of this study (a) indicate the relevance of thermal convective motions in icy moons' oceans, and (b) offer a possible framework to estimate where hotspots are most likely to occur, supporting future interpretations of gravity and altimetry data from missions such as JUICE and Europa Clipper. Thus, the focus was on Jupiter's icy moons—Europa, Ganymede, and Callisto—as they represent the most promising candidates for detecting active surface-subsurface interactions.

## 2. Materials and methods

### 2.1. Model equations

This work adopts a 3D formulation of Rayleigh-Bénard convection for a Newtonian fluid layer, set in a box of thickness D and horizontal sides $2\pi$D. Periodic boundary conditions are used along the two horizontal axes $x$ and $y$ at $x = 0, 2\pi$D and $y = 0, 2\pi$D. With periodic boundary conditions, the net lateral fluxes of mass, momentum and heat are zero, so the domain-mean budgets close without sidewall contributions, $\phi(x + 2\pi D, y, z, t) = \phi(x, y, z, t)$, $\phi(x, y + 2\pi D, z, t) = \phi(x, y, z, t)$. This configuration approximates a local patch of a large, horizontally homogeneous ocean. Boundary conditions on temperature ~~salinity~~ and velocity along the vertical directions $z$ at $z = 0$ and $z =$ D are discussed below. Gravity is aligned with the vertical direction and points opposite to the $z$ axis, i.e., $\vec{g} = (0, 0, -\mathrm{g})$. The model includes rotation, that can be set in any direction in the $y$-$z$ plane, $\vec{\Omega} = (0, \Omega_y, \Omega_z)$. The fluid is considered incompressible, and the model uses the Boussinesq approximation (Rayleigh, 1916; Chandrasekhar, 1961).

The system of model equations is:

$$\nabla \bullet \boldsymbol{u} = 0 \qquad \text{Continuity equation} \tag{2.1}$$

$$\frac{\mathrm{D}\boldsymbol{u}}{\mathrm{Dt}} = -\frac{1}{\rho_0}\nabla \mathrm{p} - 2\boldsymbol{\Omega} \times \boldsymbol{u} + \boldsymbol{g}\,\alpha\,\mathrm{T} + \nu\nabla^2\boldsymbol{u} \qquad \text{Momentum equation} \tag{2.2}$$

$$\frac{\mathrm{DT}}{\mathrm{Dt}} = \kappa\nabla^2\mathrm{T} \qquad \text{Heat equation} \tag{2.3}$$

where T is temperature, $\boldsymbol{u} = (\mathrm{u}, \mathrm{v}, \mathrm{w})$ is the three-dimensional fluid velocity, with w positive upward along the vertical, $\rho_0$ is a reference density and $\alpha$ is the coefficient of thermal expansion. In accordance with the (so-called "strong") Boussinesq approximation, kinematic viscosity $\nu$ and thermal diffusivity $\kappa$ are assumed constant and density fluctuations around $\rho_0$ depend linearly on temperature fluctuations. In the current preliminary exploration, the study refers to pure water properties.

The above equations admit a static (time-independent), horizontally homogeneous and conduction-dominated solution with linear dependence of temperature along the vertical and null velocities. Two important non-dimensional parameter for the above set of equations are the Prandtl number, $Pr = \nu/\kappa$ and the Rayleigh number ($Ra$), which for imposed-flux conditions is classically defined as $\mathrm{Ra} = \frac{\alpha \mathrm{g} \mathrm{D}^4 \mathrm{F}}{\nu \kappa^2 \rho c_p}$ where F is the imposed average heat flux across the horizontal boundaries (Choblet et al., 2017). The Rayleigh number controls the stability of the static

solution and more generally the characteristics of the flow; in particular, for values of *Ra* above a critical threshold (between about 650 and 2000 depending upon the boundary conditions on temperature and velocity, see e.g. Chandrasekhar, 1961), the static conductive solution becomes unstable and convective motions ensue. Typically, turbulent convective plumes emerge for values of the Rayleigh number in excess of $10^4$ (e.g. Parodi et al., 2004) (Fig. 1).

### 2.2. Boundary conditions

We assume that the simulated portion of the ocean spans the whole ocean depth between the lower boundary, set as z = 0 at the bottom ocean-ice (or rock) interface and the upper boundary, set as z = D at the average position of the upper ocean-ice interface. For all Jupiter's icy moons, it can be reasonably assumed that phase changes do not occur at the lower boundary, whether composed of a high-pressure ice layer or a rocky mantle. In contrast, possible melting/freezing at the upper ice layer must be considered.

#### 2.2.1. Bottom boundary (seafloor)

As mentioned, no phase-changing processes are assumed at z = 0. Velocity is considered null at the sea floor. The boundary conditions then become:

Velocity:

$$w_{bottom} = 0; u_{bottom} = v_{bottom} = 0 \qquad \text{No slip} \tag{2.4}$$

Temperature:

$$-\rho\, c_p \kappa \frac{\partial T}{\partial z} = F \qquad \text{Fixed flux} \tag{2.5}$$

where F is an imposed, spatially homogeneous heat flux at the bottom of the ocean. The choice of fixed-flux lower boundary condition is due to the fact that the temperature at the bottom of the ocean is not known, while the internal heat flux can be estimated through models that account for tidal heating and radiogenic heat production (Lebec et al., 2023), and, supposing a statistically stationary thermal state of the ocean and of the upper ice cover, it is mirrored by the value of the heat flux emerging from the external surface of the icy moon. Here, we assume the bottom heat flux to be constant in the simulation box, but in principle it could assume a different value for boxes located at different latitudes.

#### 2.2.2. Upper boundary (top of the ocean)

Observations and thermal models suggest the presence of a surface ice I layer above the ocean, with an average thickness $< H >$. At the top of this layer, the temperature is fixed at the orbit-mean value $T_S$ that may vary with latitude. At the contact between ice and water, which corresponds to the upper boundary of the ocean, the temperature at the ice-water interface is fixed at the pure ice melting temperature $T_f$, here for simplicity assumed at 273.15 K (other values generated by the high pressure of the overtopping ice layer do not qualitatively change the results). Water velocity is considered null at the contact with the ice (assuming the possible ice motions to be much slower than those of the water). With this choice, the boundary conditions at the top of the ocean become:

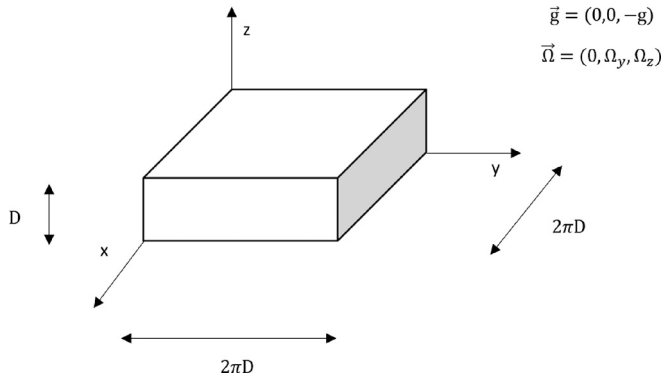



**Fig. 1.** Schematic configuration of the Rayleigh-Bénard model setup.

Velocity:

$$w_{top} = 0; u_{top} = v_{top} = 0 \qquad \text{No slip} \tag{2.6}$$

Temperature:

$$T|_{z=top} = T_f \qquad \text{Fixed temperature} \tag{2.7}$$

Here, we impose w = 0 because, as it will be explicitly shown in section 2.5, the ice dynamics is much slower than those of the ocean and thus the speed of ice edge motions can be neglected on the time scale of ocean motions. This choice is consistent with the fact that ice thickness variations are computed in post-processing.

### 2.3. Static conductive solution

For the static solution, all variables are homogeneous on the horizontal, the top of the ocean is at z = D and heat is transferred by conduction. Inside the ocean, the static temperature profile is linear along the vertical,

$$T_{stat}(z) = \frac{F}{\rho\, c_p \kappa}(D - z) + T_f \tag{2.8}$$

and the heat flux from the ocean at the upper boundary is $F_{OC} = F$. Using a simple diffusive heat transfer in the upper ice layer, thus neglecting possible convective motions in the ice, we can write

$$F_{OC} = F = F_{ICE} = \rho_{ICE}\, c_{p,ICE}\, \kappa_{ICE} \frac{T_f - T_S}{H_{stat}} \tag{2.9}$$

which determines the ice thickness $H_{stat}$ for the static solution for given values of F and $T_S$. Using the estimated parameter values reported in Table 1 below for Ganymede, we obtain that $H_{stat}$ is about 69 km, in agreement with the estimated thickness (Table 1). Notice, also, that eq. (2.8) allows for determining the temperature at the lower ocean boundary (z = 0) in the static case, to be discussed further below:

$$T_{bottom} = T_{stat}|_{z=0} = \frac{FD}{\rho\, c_p \kappa} + T_f \tag{2.10}$$

### 2.4. Dynamics at the water-ice interface

At the upper ocean boundary, when only conduction is present, the heat flux is constant in space and time $\langle F_{OC} \rangle = F$. When convection is present, the heat flux can vary in space and time and can locally differ from the average value. In this case, localized phase changes can occur as ice may either freeze or melt depending on the heat flux transported by the oceanic convection. As a result, the upper ice-ocean boundary will become modulated in space and time. If the heat flux from the ocean is locally larger than the static value F, ice will melt, while if it is lower than F, water will freeze, and the ice thickness will locally increase. In statistically stationary conditions (i.e., the average heat flux from the lower boundary equals that emerging from the surface of the satellite) the spatial average of the local heat flux from the ocean must be equal to F, so the average thickness of the upper ice layer, $<H>$, will remain equal to $H_{stat}$.

In the present formulation, we adopt a simplified description based of the local ice thickness dynamics as a function of the heat flux supplied by convection. We assume that $\eta$ is a local fluctuation of the boundary at the ice-ocean interface, assumed positive upward, generated by local ice melting/freezing dynamics. The local ice thickness becomes $H \leq H > - \eta = H_{stat} - \eta$ (notice that when $\eta$ is positive, the local ice thickness is smaller

**Table 1**
Values of the main parameters adopted in the numerical simulation, for the case of Ganymede. In brackets, the source of the information.

| Parameters | Values | Adopted value |
|---|---|---|
| Ocean depth (D) | 300 km (Bire et al., 2022)<br>361 km (Soderlund, 2019) | 300 km |
| Average ice thickness (H) | 70 km (Soderlund, 2019) | 70 km |
| Average surface temperature ($T_S$) | 120 K (Spohn and Schubert, 2003)<br>100 K (Journaux et al., 2020) | 120 K |
| Heat flux (F) | 40 mW/m$^2$(Lebec et al., 2023) | 40 mW/m$^2$ |
| Kinematic viscosity of water, ($\iota$) | molecular (at 274 K):<br>$1.74 \times 10^{-6}$ m$^2$/s | not used |
| Eddy viscosity of water,( $\nu_E$) | unknown | 35 m$^2$/s |
| Thermal diffusivity of water, ($\kappa$) | molecular (at 274 K):<br>$0.14 \times 10^{-6}$ m$^2$/s | not used |
| Eddy thermal diffusivity of water, ($\kappa_E$) | unknown | 35 m$^2$/s |
| Kinematic viscosity of the ice ($\kappa_{ICE}$) | $10^{-5}$ m$^2$/s | $10^{-5}$ m$^2$/s |
| Rotation rate ($\Omega$) | $1 \times 10^{-5}$s$^{-1}$<br>(Soderlund, 2019) | $4 \times 10^{-7}$s$^{-1}$ |
| Water density ($\rho_W$) | $1.0 \times 10^3$ kg/m$^3$ (Spohn and Schubert, 2003, Hussmann et al., 2015) | $1.0 \times 10^3$ kg/m$^3$ |
| Ice density ($\rho_{ICE}$) | $1.0 \times 10^3$ kg/m$^3$(Spohn and Schubert, 2003, Hussmann et al., 2015) | $1.0 \times 10^3$ kg/m$^3$ |
| Gravity (g) | 1.58 m/s$^2$ (Spohn and Schubert, 2003)<br>1.6 m/s$^2$ (Lebec et al., 2023) | 1.58 m/s$^2$ |
| Specific heat capacity of water ($c_p$) | $3 \times 10^3$ J/(kg K)<br>(Soderlund, 2019) | $3 \times 10^3$ J/(kg K) |
| Specific heat capacity of ice ($c_{p_{ICE}}$) | $1.8 \times 10^3$ J/(kg K) (Soderlund, 2019) | $1.8 \times 10^3$ J/(kg K) |
| Thermal expansivity ($\alpha$) | $2.5 \times 10^{-4}$ K$^{-1}$<br>(Bire et al., 2022)<br>$1.5 \times 10^{-4}$ K$^{-1}$<br>(Lebec et al., 2023) | $2.5 \times 10^{-4}$ K$^{-1}$ |

and we have discarded possible changes of the external ice surface).

The heat flux at the top of the ocean should then be represented by

$$F_{OC} = -\rho\, c_p\, \kappa \left.\frac{\partial T}{\partial z}\right|_{z=D+\eta}$$

In principle, this quantity should be evaluated at the ice-water interface located at $z = D+\eta$, which generates a so-called Stefan problem (Crank, 1984). However, given that in general we are looking for cases where the local fluctuation in ice thickness is very small, that is $|\eta| << H_{stat} < D$, for simplicity the boundary conditions are applied at $z = D$. Thus, it is imposed that:

$$F_{OC} = -\rho\, c_p\, \kappa \left.\frac{\partial T}{\partial z}\right|_{z=D} \tag{2.11}$$

The heat flux coming from the ocean, then, must equal the heat flux going through the ice plus the heat input or output associated with the phase changes of ice:

$$F_{OC} = -\rho\, c_p\, \kappa \left.\frac{\partial T}{\partial z}\right|_{z=D} = F_{ICE} - L\, q \tag{2.12}$$

where $L$ is the latent heat and $L\,q$ the latent heat flux that is negative if heat is absorbed by the ice (ice melting) and positive if new ice freezes from the ocean water. For ice melting/freezing, $q$ can be written as:

$$q = \rho_{ICE}\, \frac{dH}{dt} \tag{2.13}$$

where $\frac{dH}{dt}$ is the variation in the thickness of the ice layer above the ocean. The equation for the time evolution of upper ice layer thickness can then be written as:

$$-\rho\, c_p\, \kappa \left.\frac{\partial T}{\partial z}\right|_{z=D} + L\ \rho_{ICE}\, \frac{dH}{dt} = \rho_{ICE}\, c_{p,ICE}\, \kappa_{ICE}\, \frac{T_f - T_S}{H} \tag{2.14}$$

This formulation can generate local deviation of the ice thickness from its mean value $H_{stat}$. As mentioned above, it is assumed that such deviations are small compared with both $H_{stat}$ and $D$ and thus, after linearizing the equation around $H_{stat}$ and consistent with applying the boundary conditions at $z = D$, eq. (2.13) becomes:

$$-\rho\, c_p\, \kappa \left.\frac{\partial T}{\partial z}\right|_{z=D} - L\ \rho_{ICE}\, \frac{d\eta}{dt} = \rho_{ICE}\, c_{p,ICE}\, \kappa_{ICE}\, \frac{T_f - T_S}{H_{stat}} \left(1 + \frac{\eta}{H_{stat}}\right) \tag{2.15}$$

where $H = H_{stat} - \eta$ and we used the fact that $H_{stat}$ is constant.

### 2.5. Non-dimensional formulation

The non-dimensional formulation is obtained by using as space scale the ocean depth, $D$, and for time the thermal diffusive time scale, $\tau_{TH} = D^2/\kappa$. The thermal diffusive time indicates the time that heat takes to be transferred from the lower to the upper ocean boundary by pure thermal diffusion, and it usually much longer than the typical heat transfer time due to turbulent convective dynamics, $\tau_{dyn} = (\tau_{TH}\tau_{vis}/Ra)^{1/2}$ when the Rayleigh number is large. Here, $\tau_{vis} = D^2/\nu$ is the viscous time.

Since adding a constant to the temperature does not change the equations (temperature appears only as a difference/derivative in the dynamical equations), from now we shall fix $T_f = 0$ in the non-dimensional formulation eq. (2.10). The equations thus become (from now on, otherwise specifically indicated, all variables are non-dimensional):

$$\nabla \bullet \boldsymbol{u} = 0 \qquad \text{Continuity equation} \tag{2.16}$$

$$\frac{D\boldsymbol{u}}{Dt} = -\nabla \mathrm{p} - 2\Omega' \hat{\boldsymbol{r}} \times \boldsymbol{u} + \mathrm{Pr\ Ra}\ T\, \hat{\boldsymbol{z}} + \mathrm{Pr}\ \nabla^2 \boldsymbol{u} \qquad \text{Momentum equation} \tag{2.17}$$

$$\frac{DT}{Dt} = \nabla^2 T \qquad \text{Temperature equation} \tag{2.18}$$

with thermal boundary conditions

$$T|_{z=1} = 0 \qquad \text{Fixed temperature} \tag{2.19}$$

and

$$-\left.\frac{\partial T}{\partial z}\right|_{z=0} = 1 \qquad \text{Fixed flux} \tag{2.20}$$

In eq. (2.16), $\Omega'$ is the moon's rotation rate in units of the thermal diffusive time.

With these choices, the non-dimensional equation for the ice thickness becomes:

$$\frac{d\eta}{dt} = A \left[ -\left.\frac{\partial \theta}{\partial z}\right|_{z=1} + 1 - B\left(1 + \frac{\eta}{H_{stat}}\right) \right] \tag{2.21}$$

where we have written

$$-\left.\frac{\partial T}{\partial z}\right|_{z=1} = 1 - \left.\frac{\partial \theta}{\partial z}\right|_{z=1.}$$

and $\theta$ is the temperature fluctuation with respect to the static solution at z = 1, recalling that the non-dimensional heat flux of the static solution is equal to 1.

The two (positive) non-dimensional parameters $A$ and $B$ are (note that the constants in their definitions below are dimensional):

$$A = \frac{FD}{L\,\rho_{ICE}\kappa} \tag{2.22}$$

$$B = \frac{\rho_{ICE}\,c_{p,ICE}\,\kappa_{ICE}}{\rho c_p \kappa}\,\frac{T_f - T_s}{H_{stat}} \tag{2.23}$$

It is worth noting that the parameter A introduced in eq. (2.22) can be expressed as the inverse of the Stefan number as defined by Gastine and Favier (2025), $A = St^{-1}$. It is the ratio between latent and sensible heat and it determines how much heat is required to have a phase change with respect to that required to change temperature. Further details will be provided in the following section.

The two parameters $A$ and $B$ can be estimated from the typical values available in the literature for icy moons (see Table 1 for Ganymede). In general, $B$ turns out to be of order 1, and thus both terms on the right side of the ice evolution equation are of the same order of $A$. Estimates of $A$ give a value of the order of $10^{-6}$. This indicates that the time scale over which the ice shell thickness varies is much slower than the time scales over which ocean dynamics take place.

In case the heat flux $-\frac{\partial\theta}{\partial z}\Big|_{z=1}$ is constant in time at a given location, eq. (2.20) admits a stable, local stationary equilibrium, obtained by imposing $d\eta/dt = 0$. Such equilibrium is given by

$$\frac{\eta}{H_{stat}} = \frac{1}{B}\left(1 - \frac{\partial\theta}{\partial z}\Big|_{z=1}\right) - 1 \tag{2.24}$$

Of course, in turbulent conditions the convective heat flux at a point is expected not to be constant in time and the local ice thickness variation will usually be much smaller. In particular, at any given time the ice thickness variation at a point in space will be the product of the whole past history of heat flux variations at that point, as indicated by eq. (2.20).

### 2.6. Computational approach

Fluid dynamical convection simulations have been performed using RBsolve, a CFD code for Rayleigh-Benard problem simulation in the Boussinesq approximation (Parodi et al., 2004). The code is written in FORTRAN and solves a system of coupled equations for momentum and temperature. All variables are non-dimensional. This code adopts a 3D Cartesian box of a Newtonian fluid with depth $D = 1$, square horizontal section of side $L = 2\pi$, and horizontally periodic boundary conditions in the x and y directions. The fluid dynamical equations are integrated numerically using a pseudospectral method in the horizontal directions with 2/3 dealiasing, while second-order finite differences are used in the vertical. A third-order fractional step method is adopted in time (Kim and Moin, 1985). We use a resolution of $128^2$ grid points in the horizontal and 129 vertical levels. The spatial resolution in the vertical is more refined close to the top and bottom plates in order to better resolve the boundary layers (Grötzbach, 1983). Numerical parallelization is performed by partitioning the domain in horizontal slices, using the MPI paradigm.

One important problem of this type of numerical simulation is that the typical range of spatial scales involved. These span from the smallest scales associated with molecular diffusion to the scales of ocean motions (hundreds of kilometers); such range cannot be represented in a single simulation. Thus, numerical simulations using the value of molecular viscosity and thermal conductivity typically model only a few cubic meters of fluid, while simulations dealing with much larger scales are forced to use a form of closure of the small-scale motions, parameterizing the dynamics at the unresolved scales (Pope, 2000). The work presented here focuses on the dynamics of the convective plumes at a scale of a few km, thus neglecting the small turbulent flow structures. From this perspective, $\nu$ and $\kappa$ must be considered as "eddy" quantities, $\nu_E$ and $\kappa_E$, much larger than the molecular values, as they represent the effects of small-scale fluid turbulence through a simplified eddy-viscosity closure. Under this assumption, since both momentum and heat diffusion are driven by smaller-scale turbulence acting uniformly on them, it follows that $\nu_E = \kappa_E =$ K, leading to a value of the "eddy" Prandtl number $Pr = \nu_E / \kappa_E = 1$.

The equation for the ice thickness time evolution (2.20) is numerically integrated once the temperature and velocity fields have been computed. Here, another problem emerges, since the value of A in eq. (2.22) is usually very small; the time scale of the ice reaction is correspondingly much longer than the time scale of ocean convection. For this reason, in this first exploration we do not include the feedback of the changes in the upper ice cover on the ocean dynamics, consistent with the assumption that ice thickness variations are small. To provide realistic results, we run the ocean simulation starting from random initial conditions until a statistically stationary state for energy and heat transfer is reached and the initial transient has ended. The simulation of the ice dynamics is started only after this moment. During the ice response integration we then use the full time-dependent ocean heat flux, that is, the temperature gradient computed by the convection simulations at each time. We estimate the heat flux at the upper boundary of the ocean at the ice-ocean boundary, here represented by the two uppermost grid points in the vertical numerical discretization.

## 3. Results

The methodology outlined above is applied to a portion of the subsurface ocean of an icy moon. Since this study is part of the JUICE Phase E project, we specifically explore how the model behaves when configured with the parameters representative of Ganymede. Several studies have attempted to constrain Ganymede's internal structure by integrating gravity field measurements with compositional and thermal evolution models (Bire et al., 2022; Bland et al., 2009; Hussmann et al., 2015; Journaux et al., 2020; Lebec et al., 2023; Soderlund, 2019; Soderlund et al., 2020; Spohn and Schubert, 2003; Vance et al., 2014). These efforts have produced estimates for the physical properties of the oceanic and ice layers, including ocean depth, ice layer thickness and surface temperature, and internal heat flux. Although the local plane-layer model adopted in this study cannot capture the whole of Ganymede's ocean, and other limitations of the fluid model allow only for a simplified conceptual description of the ocean-ice dynamics, the parameter choice adopted here provides insight into how turbulent convection alone may drive basal melting or freezing under conditions consistent with those expected on Ganymede. Table 1 reports the main parameters adopted in the simulations.

With these parameters, we obtain the parameter values $A = 1.03 \times 10^{-6}$ and $B = 1$ in eqs. (2.21 and 2.22).

Since A is the inverse of the Stefan number, we can write:

$$St = \frac{L}{c_p \Delta T} = 1.03 \times 10^6 \gg 1 \tag{3.1}$$

This confirms that ice responds to timescales that are extremely slow compared to those of water. Hence, assuming a fixed water–ice interface and neglecting feedback effects is consistent within our framework. Although this may appear as a limitation when investigating longer timescales, A (and thus the Stefan number) acts essentially as a time–scale factor (at least when $A << 1$). Variations of A modify only the characteristic timescale of the ice response, while the spatial patterns of interface morphology remain similar. This implies that our results can be extrapolated to geological timescales, as further illustrated in Appendix B.

Another key step concerns kinematic viscosity. If we used the molecular values for viscosity and thermal diffusivity and the estimated parameter values for Ganymede reported in Table 1, together with the definition of the temperature difference in eq. (2.8), we would obtain a value of the Rayleigh number of the order of $10^{24}$, owing to the huge depth of the ocean. This shows that even for the small heat flux observed for icy moons, the ocean should be in a fully turbulent state, see the

Discussion for further comments on these values.

On the other hand, here we have a horizontal resolution of about 5 km, and thus we are forced to use eddy values for kinematic viscosity and thermal diffusivity. Such values for the ocean of Ganymede are unknown. For the Earth's ocean, the value of eddy viscosity depends on the spatial scale at which the motions are unresolved. As an example, for the open ocean such values are estimated to vary from $10^{-3}$ $m^2/s$ to 1 $m^2/s$ for small-scale turbulence (Ledwell et al., 1998; Nencioli et al., 2013). For simplified ocean models in the quasigeostrophic approximation, on the other hand, the assumed eddy viscosity in general decreases with increasing model resolution, and it can reach values well above 100 $m^2/s$ for low resolution (Maulik and San, 2016). Given the horizontal resolution adopted here, we fixed an eddy value $\nu_E$=$\kappa_E$=K = 35 $m^2/s$. Even for this relatively large value, we obtain a value of the "eddy" Rayleigh number of the order of $10^6$, orders of magnitude above the stability threshold for a conductive solution. The fluid motions in the ocean layer are thus expected to be in a turbulent convective regime dominated by convective plumes with horizontal scales of several km (Marshall and Schott, 1999; Paluszkiewicz et al., 1994; Parodi et al., 2004), complemented by sub-grid scale turbulent eddies which are unresolved here.

The dynamics of the oceanic portion and the associated ice response were simulated for a total of one diffusive time, $D^2/k$, in a statistically stationary turbulent convective regime. From the values in Table 1, this corresponds to about 80 terrestrial years. In turn, this corresponds to about 1000 dynamical times, which for our choice $\nu_E = \kappa_E =$ K is defined as $\tau_{E,dyn} = \tau_{E,TH}/Ra^{1/2}$. The dynamical time is roughly equivalent to the time a single fluid parcel takes to cross the depth of the ocean due to convection. Given the above values, the dimensional dynamical time is about 29.8 terrestrial days, which implies convective speeds of almost 10 km/day, more than an order of magnitude larger than the strongest ocean vertical velocities of up to 170 m/day observed at submesoscale fronts on Earth (Zhu et al., 2024).

The angle between the rotation axis and the horizontal plane represents the tilt of the rotation axis, consistent with representing the local dynamics and water-ice interactions at different latitudes within a rotating fluid shell. Notice, also, that the non-dimensional rotation rate simulated here is $\Omega' = 500$, corresponding to a rotation period of about 360 terrestrial days, more than an order of magnitude larger than the rotation period of Ganymede. We were forced to use this value to assure numerical stability of the simulations; for further consideration on this issue see the Discussion section.

Fig. 2 reports the results of the simulations after one diffusive time for three different latitudes, namely at the pole (rotation axis pointing in the local vertical direction), midlatitudes (rotation axis inclined at 45° with respect to the local vertical) and the equator (rotation axis

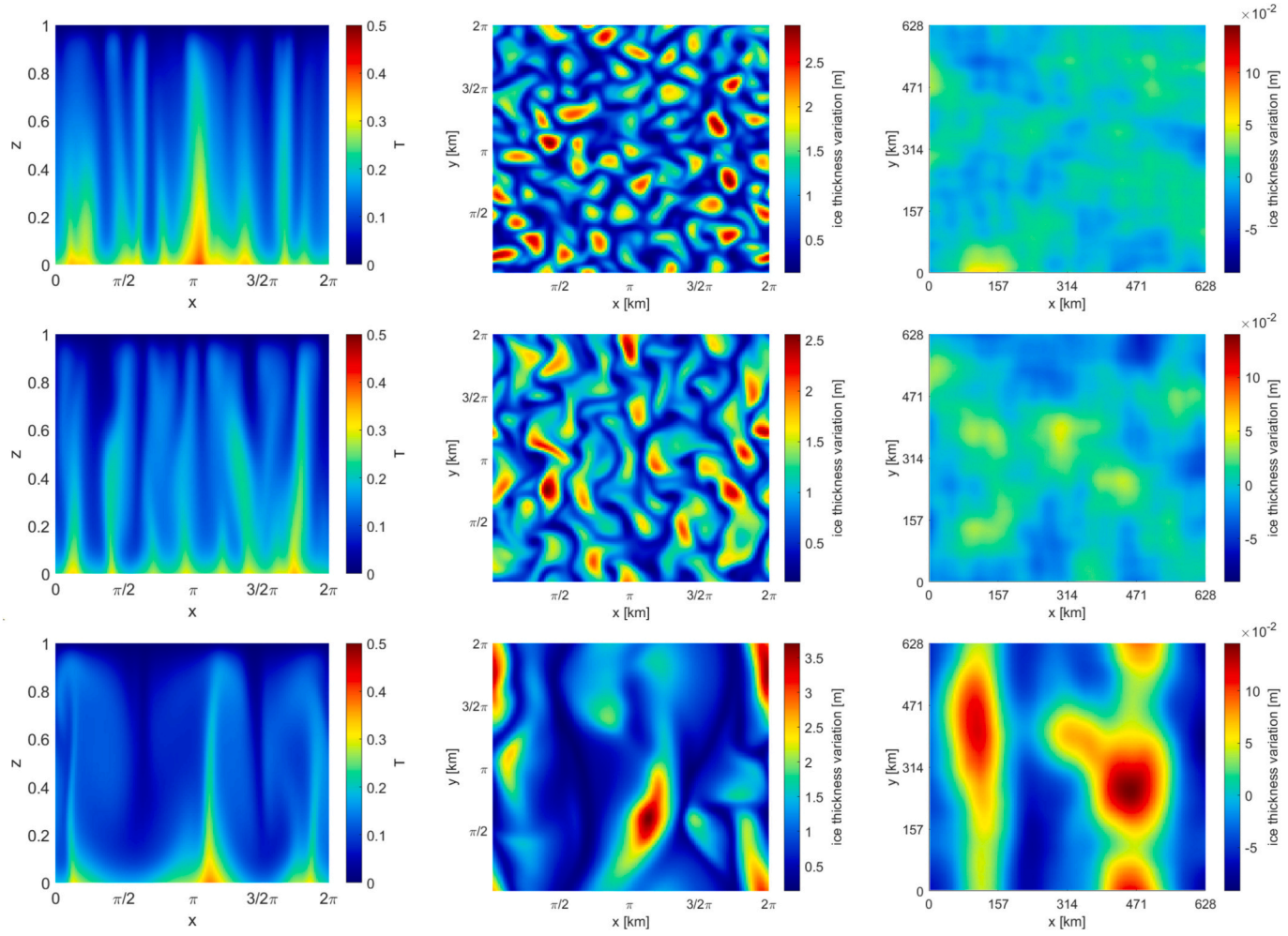



**Fig. 2.** Left panels: Vertical sections in the x-z plane of the temperature field in the ocean at y = π in the 3D turbulent, rotating convective simulations. Central panels: Horizontal sections of the non-dimensional heat flux at the water-ice interface. The non-dimensional heat flux is the total heat flux divided by the conductive heat flux. Right panels: Ice thickness variation in meters, in these panels the horizontal dimension is also dimensional. All snapshots are taken after about 80 years of simulation, corresponding to one thermal diffusive time and 1000 dynamical times. Upper panels: poles; middle: midlatitudes; lower: Equator. In the middle and lower panels, North is pointing upwards.

perpendicular to the local vertical). From this figure, several indications can be drawn. At the poles, convective plumes generate small, mobile hotspots, resulting in a maximum ice thickness difference between regions of ice melting and ice freezing of approximately 0.10 m after 80 yr. At mid-latitudes, a slight shear effect due to the rotation becomes evident, elongating the structures in the North-South direction, consistent with previous findings (Julien and Knobloch, 1998; Novi et al., 2019; Currie et al., 2020). However, even in this region, the resulting hotspots remain relatively small, leading to a similar maximum freezing/melting difference of about 0.12 m. At equatorial latitudes, rotational shear plays a more significant role, causing the fluid to organize into alternating bands of warmer and cooler regions, significantly elongated along the North-South direction. This behavior leads to the formation of larger hotspots and more intense ice melting/freezing, reaching more than 0.24 m of ice thickness difference between melting and freezing areas over the same timescale.

If the plume pattern and the corresponding heat flux shown in Fig. 2 were static in time, then using eq. (2.23) one would obtain a maximum

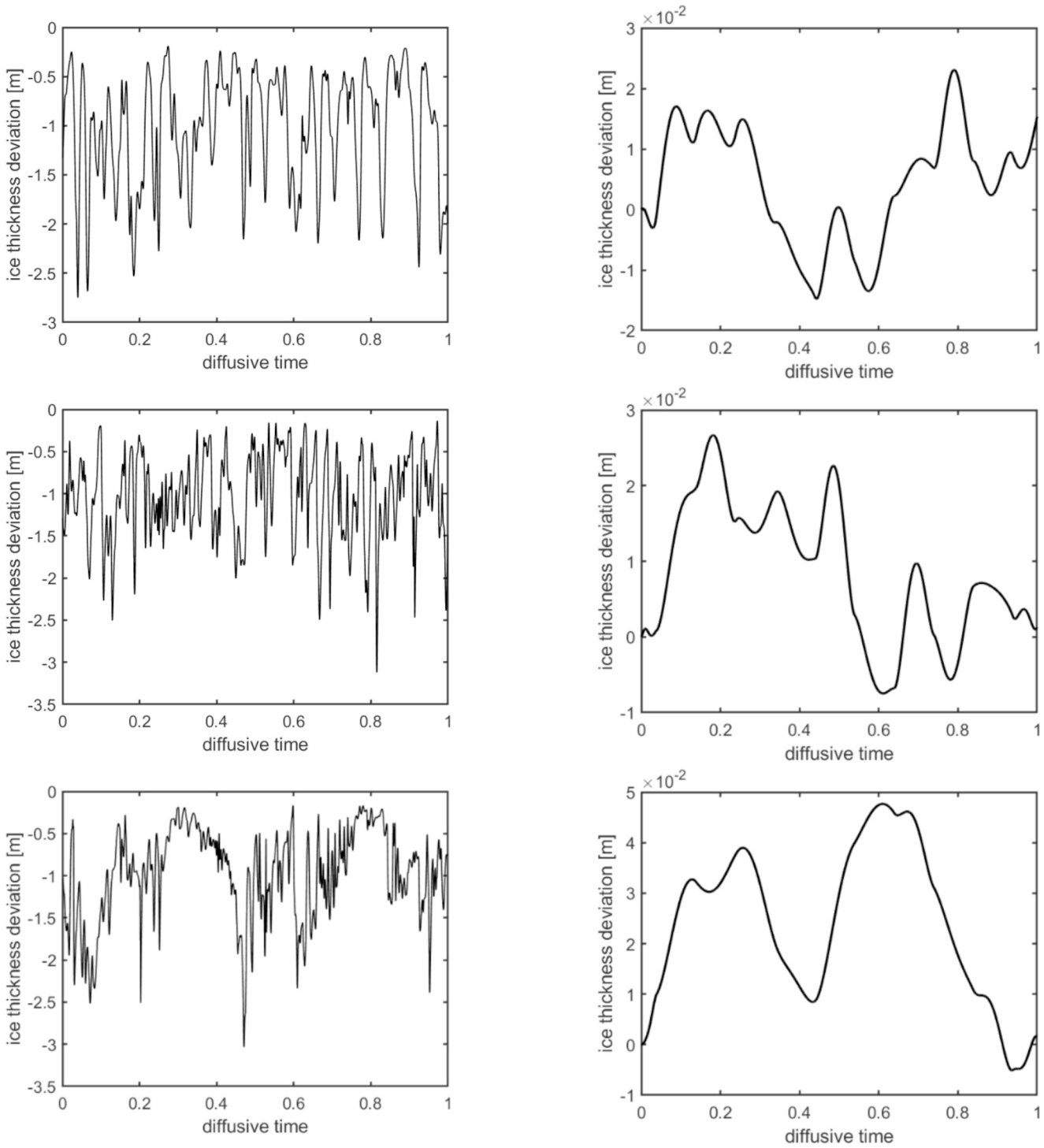



**Fig. 3.** Left: Time series of the non-dimensional heat flux at the water-ice interface in the 3D turbulent, rotating convective simulations, at the central point in the domain. The non-dimensional heat flux is the total heat flux divided by the conductive heat flux. Right: Ice thickness variation in meters at the same point. Upper panels: poles; middle: midlatitudes; lower: Equator.

ice deviation which in due course could melt the whole ice layer in the areas of strongest heat flux: for example, in the case of equatorial latitudes, the heat flux in the red spots around ($\pi$, $\pi/2$) is more than twice the average heat flux. In general, however, the convective patterns tend to move around in the domain, albeit relatively slowly compared to the dynamical time, and this means that at any given point the final ice thickness perturbation generated by convection will be much smaller, as it will be determined by a weighted integral over the past history of heat flux at that point. To illustrate this issue, in Fig. 3 we show the time series of the ocean heat flux at the ice-ocean boundary and of the corresponding ice thickness perturbation for three selected points in the domain, for the three latitudes already considered in Fig. 2.

Interesting information concerns the root mean square (rms) variation of ice thickness over the whole spatial domain. Fig. 4 shows such rms variations calculated over the horizontal plane ($2\pi$, $2\pi$), corresponding to about $628 \times 628$ square kilometers, for the three latitudes considered. Also from this metric, equatorial regions emerge as those where turbulent convective plumes, organized into shear structures by the rotation, can have the strongest effect.

Fig. 4 illustrates what is already clear from the relative values of the ocean and ice response time scales. After one diffusive time, the r.m.s. variation of the ice thickness is still growing, and it is expected to do so for much longer times. On the other hand, we cannot simulate the 3D turbulent dynamics for tens of thousands of diffusive times. One partial answer to the long-term growth of the ice variation comes from noticing that the most relevant response is observed at equatorial latitudes. Here, the rotation axis is perpendicular to the local vertical direction (where gravity acts), and the net effect is a tendency to make the fluid flow two-dimensional in the x-z plane, perpendicular to the rotation axis (Hussmann et al., 2015).

## 4. Discussion and conclusions

In the Earth's ocean, the main heat source is related to the absorption of solar radiation in the upper 200 m of the water column. This leads to a generally stable stratification, and buoyancy-driven convective motions are generally confined to small and specific areas in polar regions and in some other special locations. The situation on an ice-topped ocean is, however, very different. Here, the main buoyancy source is associated with the heat flux from the lower ocean boundary, generated by both internal heating from radioactive decay in the silicate mantle and tidal heating. In this case, the ocean can become unstably stratified in large areas, and strong convective motions can ensue.

The first question concerns the intensity of such vertical convective motions. A first observation is that the very small heat flux from the lower ocean boundary estimated for Ganymede (and similar values are found for other icy moons) could suggest a minor effect on thermal convection. On the other hand, using the values indicated in Table 1 and even including the growth of kinematic viscosity and thermal diffusivity with pressure, such a small heat flux from the bottom generates values of the Rayleigh number well in excess of $10^{20}$, owing to the large depth of the ocean. These values of the Rayleigh number indicate the presence of a strongly turbulent convective state for these ice-capped oceans. In this sense, the icy moon's oceans can have fluid dynamical conditions that are completely different from those of Earth's oceans.

This strong turbulence generates both large and intermediate scale convective flows and strong small-scale turbulent motions. Given the current impossibility of simulating the whole range of scales from the smallest turbulent swirls to ocean-scale circulations, here we have used a simplified parameterization of the sub-grid scale turbulence, adopting rather large values of the eddy viscosity and thermal diffusivity, namely, $\nu_E = \kappa_E = 35\ \mathrm{m}^2/\mathrm{s}$. But even with this choice, the immense ocean depth leads to values of the Rayleigh number of the order of $10^6$, indicating that also the larger-scale flows are in a fully turbulent convective regime, with the fluid motions dominated by turbulent, localized convective plumes with horizontal scales of the order from a few to some tens of km. These plumes carry hot fluid upward, towards the overtopping ice boundary and cold fluid downward.

The convective plumes generate spatial and temporal fluctuations in the heat flux reaching the top of the ocean, at the ice-water interface. Assuming the average ice thickness to be in a statistically stationary state, determined by the average heat flux from the ocean and the heat transfer speed across the ice, the convection-induced fluctuations generate local ice melting (when the heat flux is larger than average) or freezing (when the heat flux is less than average). In turn, this generated variations in the ice thickness on scales of the order of the convective structures, say from a few to several tens of kilometers.

The presence of vigorous km-scale convective plumes makes the numerical simulation of icy moons' oceans quite challenging, as large-scale, global circulation models(Ashkenazy and Tziperman, 2021; Bire et al., 2022; Soderlund et al., 2014) do a good job in representing the overall ocean dynamics, but owing to their limited spatial resolution cannot properly represent convective motions. For this reason, here we focused our attention on the simulation of the convective processes at scales between about five to a few hundred kilometers, analyzing in particular the spatial and temporal variability of the heat flux at the upper ocean-ice boundary. To this end, we adopted a simple conceptual fluid-dynamical model describing rotating Rayleigh-Benard convection in the Boussinesq approximation in a Cartesian three-dimensional box with periodic lateral boundary conditions, assuming a constant heat flux from the ocean bottom and ice melting temperature at the upper ocean-ice boundary.

The configuration adopted here represents a localized three-dimensional portion of the ice-covered ocean, fully covering the ocean depth (assumed to be 300 km) and extending for about 628 km in the two horizontal directions. By varying the angle between the rotation axis and the gravity vector, we simulated the ocean dynamics at different latitudes. Here, we illustrated the cases for polar regions, midlatitudes, and equatorial areas, identifying significant differences in the convective dynamics emerging at these different latitudes. In all cases, strong fluid vertical velocities are obtained, which can be more

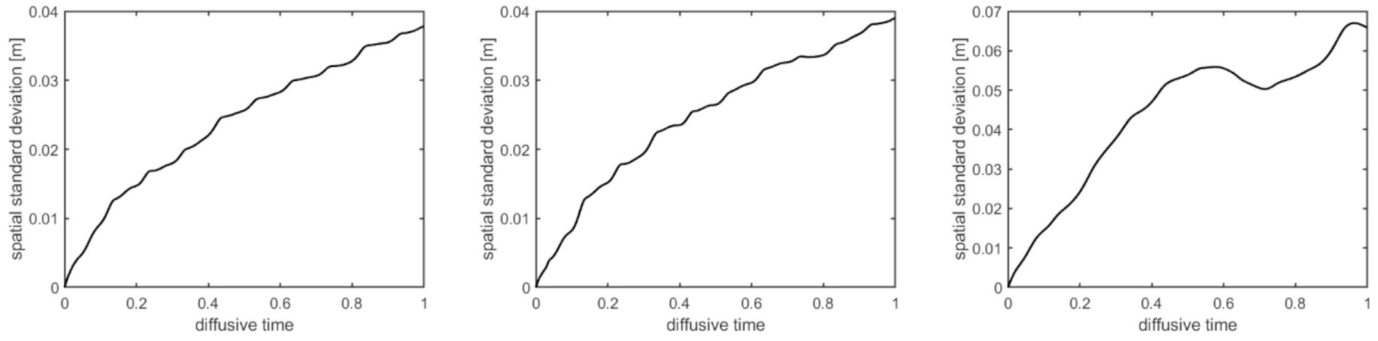



**Fig. 4.** Left: Time series of the non-dimensional rms fluctuation of the ice thickness variation (in meters) over the whole horizontal domain ($2\pi$, $2\pi$). Left panel: poles; middle: midlatitudes; right: Equator. Note the change of vertical scale for the equatorial case.

than an order of magnitude larger than the stronger vertical motions observed in Earth's oceans. A future development would be the implementation of a convection-resolving ocean circulation model in a spherical shell, with spatial resolution of at least 1 km, that should be integrated on time scales of hundreds of years. Definitely, a challenging numerical endeavor.

In our preliminary exploration, we have complemented the ocean convection simulations with a simplified, linearized description of the freeze/melt dynamics at the upper ocean-ice boundary. The issue, here, is that the ice response to the varying ocean heat flux is extremely slow (about $10^6$ times slower than ocean dynamics) and thus it depends on the past history of heat flux variations. This means that local ice thickness changes integrate in time the fluctuations induced by the convective plumes, which tend to move across the domain in the course of time. Even so, the effect is not simply averaging out the effect of the plumes; rather, well-defined patterns of ice thickness variations emerge at the different latitudes, with smaller, localized spots in polar regions and elongated shear regions in the North-South direction at equatorial latitudes. These variations in the ice thickness may take an extremely long time to fully develop (of the orders of millions of years), and it is currently unfeasible to simulate ocean convection on such time scales.

As an example, by artificially repeating the whole-time history of the simulated turbulent convection dynamics in a periodic way for 4 times, corresponding to about 160 years, and integrating eq. (2.20), the typical ice thickness perturbation between maximum melting and maximum freezing reaches about 0.5 m, and it is still growing.

An interesting effect of the ocean convective plumes is to modulate the heat flux at the base of the overtopping ice layer. If the ice layer could undergo convection, then there could be an interesting connection between the convection in the ocean and the induced convection in the ice, which would experience a non-homogeneous heat flux from below. Analogously, for each latitude we have considered a locally homogeneous heat flux from the bottom of the ocean, but if significant spatial variations of this heat flux were present, then the upward convective motions in the ocean could be rooted in the specific points of the ocean floor where the heat flux is stronger, and in turn be less free of moving around. In this case, the heat flux perturbation at the top of the ocean could be almost stationary in space, and the melting of the overtopping ice layer could be much more significant.

Clearly, the modeling frame adopted here is extremely simplified. We have adopted a simple Boussinesq approximation, while water is going to be (weakly) compressible in the lower layers of such a deep ocean. In this case, a better approximation could be the so-called anelastic approximation (Ogura and Phillips, 1962), as used in the Earth's atmosphere. On the other hand, this choice would not lead to qualitatively different results. In addition, in our simulations it was not feasible to directly implement the rotational speed estimated for Ganymede. The primary issue arises from the large depth of the ocean combined with the moon's rapid rotation, which causes instabilities in the numerical code used here. However, even a rotation that is ten to fifty times faster than the one adopted here does not qualitatively change the picture (e.g., Novi et al., 2019). At most, it should make the alternating ice thickness perturbations at equatorial latitudes even stronger, owing to the fact that in this case a stronger rotation tends to make the flow dynamics less variable along the rotation axis (Hussmann et al., 2015). Finally, we have considered a linearized version of the ice response to variations in the heat flux from the ocean, and a simplified form of the upper boundary conditions. Given the very small ice thickness perturbations observed here, this choice should not lead to relevant changes in the first stages of the ice perturbations, but it could become more important in later stages of the ice-ocean coupled evolution.

Our results can also be interpreted in the broader context of rotating Rayleigh–Bénard convection (RRBC). Previous studies (Aurnou et al., 2015; Kunnen, 2021; Ecke and Shishkina, 2023) have outlined the main dynamical regimes of RRBC, ranging from non-rotating to rotation-affected and rapidly rotating (geostrophic). Using the parameters for Ganymede's ocean adopted here, the estimated dimensionless numbers (i.e. Rayleigh, Ekman, Rossby) suggest that our simulations fall within the rotation-affected regime, rather than in the rapidly rotating geostrophic limit. This classification supports the plausibility of plume-dominated convection driving local variations at the ice–ocean boundary, consistent with turbulent and latitude-dependent structures, see Appendix A for detailed calculations. Future simulations will consider higher spatial resolution and faster rotation, to explore the rapidly-rotating turbulent regime which can be more relevant for the dynamics of Ganymede's oceanic convection, at least in the polar regions.

Even with these limitations, the present results indicate the relevance of intermediate-scale turbulent convective motions in the dynamics of icy moon's oceans. Given this, we can conclude that these oceans are very different from what is observed on Earth, where ocean convection is limited to some small and special areas. In particular, the differences observed across the three latitudes considered in this study have significant implications for the types of observations that can be conducted on icy moons. In the case of Ganymede, the most pronounced effects of thermal convection are detected at equatorial latitudes, manifested as alternating thick and thin ice bands oriented along the North–South direction.

This interpretation finds support in previous observations. Lucchetti et al. (2021) analyzed tectonic features in Ganymede's equatorial regions, known as "grooves," whose geometry and spatial distribution suggested potential connections between the surface and the underlying ocean. Their analysis indicated that these structures, identified in regions such as Uruk Sulcus, Babylon Sulci, Phrygia Sulcus, and Mysia Sulci, could penetrate the icy crust to depths of up to 100 km, potentially reaching the ocean. Our findings are consistent with this interpretation, leading us to propose that such areas may represent prime candidates for future exploration. The combination of tectonic activity and thermal convection may indicate that convection processes contributed to the formation of these features, or alternatively, that these features, in conjunction with ocean convective motions, create pathways through the ice shell that could make ocean material detectable via orbital remote sensing.

Additional support for this hypothesis comes from Tosi et al. (2023), who investigated the surface composition of Ganymede using data from the JIRAM imaging spectrometer onboard NASA's Juno mission. Their study revealed the presence of carbonates and organic compounds (e.g., aldehydes and aliphatic hydrocarbons) in equatorial terrains such as Phrygia Sulcus. These materials are typically associated with subsurface brines rather than exogenous deposition, suggesting an endogenous origin, and potentially pointing to past hydrothermal activity within the ocean.

Together, these studies support our results in identifying equatorial regions as key hotspots for future missions (such as ESA's JUICE) in the search for surface–subsurface connections. These sites may offer the best opportunity to remotely probe subsurface oceans that, while currently inaccessible, may hold critical clues about the origin and evolution of life beyond Earth.

## CRediT authorship contribution statement

**Silvia Pagnoscin:** Writing – review & editing, Writing – original draft, Visualization, Software, Methodology, Investigation, Formal analysis, Data curation, Conceptualization. **Jost von Hardenberg:** Supervision, Software, Resources, Methodology, Formal analysis. **John Robert Brucato:** Validation, Supervision, Project administration. **Antonello Provenzale:** Writing – review & editing, Validation, Supervision, Resources, Methodology, Investigation, Funding acquisition, Formal analysis, Conceptualization.

## Declaration of competing interest

The authors declare that they have no known competing financial interests or personal relationships that could have appeared to influence the work reported in this paper.

**Acknowledgements**

This work is part of the JUICE Phase E project, and it was funded by ASI under agreement n. 2023-6-HH.0, CUP F83C23000070005.

We gratefully acknowledge Alice Lucchetti and Riccardo Pozzobon for the helpful discussions on the results presented.

## Appendix A. We summarize the non-dimensional numbers used to characterize rotating Rayleigh–Bénard convection (RRBC) regimes (Ecke and Shishkina, 2022) in our configuration

Rayleigh number $$R_a = \frac{\alpha g D^4 F}{\nu \kappa^2 \rho c_p} = 10^6 \tag{A.1}$$

Prandtl number $$Pr = \nu/\kappa = 1 \tag{A.2}$$

Ekman number $$Ek = \frac{\nu}{2\Omega sin\varphi D^2} = 4.8 \times 10^{-4} \tag{A.3}$$

Convective Rossby number $$Ro = Ek\sqrt{Ra/Pr} = 0.48 \tag{A.4}$$

All values were calculated using parameters from Table 1. Combining the results obtained, our parameters set places the system in the rotation affected RRBC regime. In this regime, rotation organizes convection (e.g., plume clustering and shear-aligned features). This classification matches the morphology seen in our simulations across latitudes.

## Appendix B. Appendix

In eq. (2.21) we described the time evolution of the water–ice interface due to pure thermal convection. In eq. (2.22) we introduced the non-dimensional parameter A, which can be expressed as the inverse of the Stefan number as defined by (Gastine and Favier, 2025).

$$\mathrm{A} = St^{-1} = 1.03 \times 10^{-6} \tag{B.1}$$

This confirms that ice responds extremely slowly compared with water, and thus assuming a fixed water–ice interface and neglecting feedback effects is consistent with the large value of the Stefan number. However, previous studies (e.g., Gastine and Favier, 2025) evaluated the Stefan number for icy moons as about 40, corresponding to a much larger value of $A \approx 1 \times 10^{-2}$. The discrepancy between the two estimates arises from the different choices of $\Delta T$. Favier and Gastine selected a reference temperature difference representative of large-scale fluid motions, while we derived $\Delta T$ from parameter values consistent with our configuration, which includes strong eddy transport characterized by $\kappa \approx 35\ m^2/s$.

In our investigation, we show that A, and thus the Stefan number, acts as a time–scaling factor. To illustrate this, we integrated the interface evolution equation using a normalized time, or "Stefan time":

$$t^* = \mathrm{A}t = t/St \tag{B.2}$$

and verified that only the speed of the process changes, while the quasi-stationary ice morphology remains unaffected (as found by Ravichandran and Wettlaufer, 2021). This indicates that the Stefan number (when larger than one) essentially controls the timescale of melting/freezing, not the resulting spatial patterns at the interface. We note, however, that if additional effects such as strong feedback or salinity variations come into play, this behavior may break down.

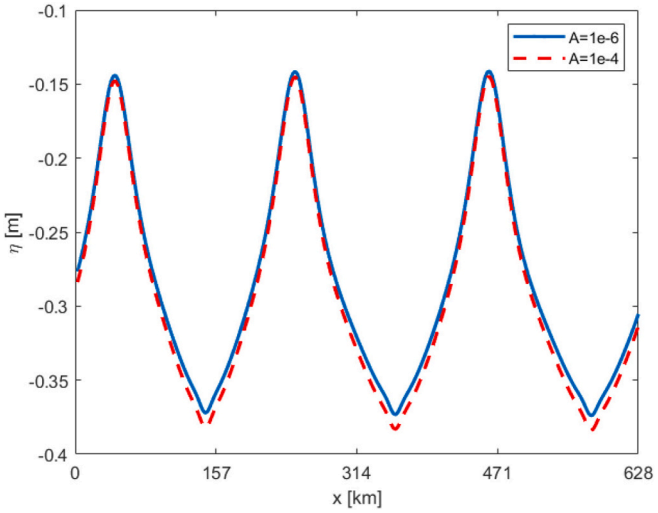



**Fig. B.1.** Ice thickness variation calculated after 1 diffusive time, using the two different Stefan time for integration, $t_1^* = A_1 t = t/St_1 = 10^{-6}$ and $t_2^* = A_2 t = t/St_2 = 10^{-4}$ similar results were obtained with different values of A.

Since our set-up is largely independent of the value of the Stefan number when $St >> 1$ (as shown above), we can extrapolate the evolution of the water–ice interface to geological timescales ($10^4 - 10^6$years) at least in 2D simulations, providing an order-of-magnitude estimate of ice thickness variations. We restrict this extension to 2D because in 3D simulations convective plumes are freer to move and not fixed in space. Nonetheless, this approach provides useful hints on long-term ice-thickness trends. From our analysis, after $10^6$ years thermal convection alone could melt up to about 3 km of ice.

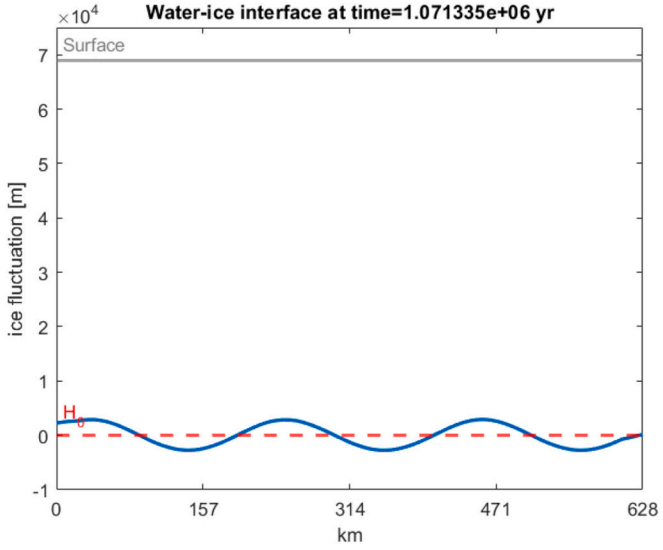



**Fig. B.2.** 2D ice thickness variation calculated after $10^6$years. Thermal convection alone can fix a lower limit of ice putative averaged melting of about 3 km over geological times.

Expanding and generalizing our findings to geological times, we reach ice topographic variations of the order of kilometers that could be detected by future gravity measurements by JUICE. These ∼3 km basal relief at the ice–ocean interface with a characteristic wavelength of ∼200 km. These structures are well positioned to be tested by JUICE: if their gravity signal maintains coherence over ≥300–500 km (spherical-harmonic degrees $\ell \lesssim$ 35–45), 3GM can robustly recover the static gravity field and, together with GALA, quantify the gravity–topography admittance even under isostatic compensation. Even at ∼200 km wavelengths ($\ell \sim 80$), where direct recovery is more demanding, the predicted relief remains potentially accessible via indirect signatures, e.g., regional spatial coherence, partial under-compensation that transfers power to lower degrees, and joint inversions that combine gravity and topography (van Hoolst et al., 2024).

In addition, we estimated the ice melting velocity using the computed solution of the equation for ice thickness variation 2.21 as follows:

$$V = \frac{d\eta}{dt} = 1.4 \text{ mm/year} \tag{B.3}$$

An upper limit for the melting velocity can also be computed. Since any upward heat loss into the ice ($F_{ICE} > 0$) or any inefficiency in delivering the ocean heat to the interface reduces the melting, an upper bound to the ice loss can be obtained when all the oceanic heat flux reaches the interface and none is conducted away through the ice ($F_{ICE} = 0$, $F_{OC} = F$). Thus, rewriting eq. 2.12 using eq. 2.13 we obtain the Stefan condition:

$$F_{OC} = F_{ICE} - L\,\rho_{ICE}\,\frac{dH}{dt} \tag{B.4}$$

$$V\rho_{ICE}L = F_{OC} - F_{ICE} \tag{B.5}$$

$$V_{max} = \frac{F}{\rho_{ICE}L} \approx \frac{0.04}{1000\left(3.34 \times 10^5\right)} \approx 1.2 \times 10^{-10}\text{m/s} = 4 \text{ mm/year} \qquad \text{s}$$

This means that in $10^6$ years ice is melted for about 4 km, in keeping with the results shown in the previous figure.

## Data availability

Data will be made available on request.

## References


Ashkenazy, Y., Tziperman, E., 2021. Dynamic Europa Ocean shows transient Taylor columns and convection driven by ice melting and salinity. Nat. Commun. 12, 6376. https://doi.org/10.1038/s41467-021-26710-0.

Aurnou, J.M., Calkins, M.A., Cheng, J.S., Julien, K., King, E.M., Nieves, D., Soderlund, K. M., Stellmach, S., 2015. Rotating convective turbulence in earth and planetary cores. Phys. Earth Planet. Inter. 246, 52–71. https://doi.org/10.1016/j.pepi.2015.07.001.

Becker, H.N., Lunine, J.I., Schenk, P.M., Florence, M.M., Brennan, M.J., Hansen, C.J., Martos, Y.M., Bolton, S.J., Alexander, J.W., 2023. A complex region of Europa's surface with hints of recent activity revealed by Juno's stellar reference unit. J Geophys Res Planets 128. https://doi.org/10.1029/2023JE008105.

Bire, S., Kang, W., Ramadhan, A., Campin, J., Marshall, J., 2022. Exploring Ocean circulation on icy moons heated from below. J Geophys Res Planets 127. https://doi.org/10.1029/2021JE007025.

Bland, M.T., Showman, A.P., Tobie, G., 2009. The orbital–thermal evolution and global expansion of Ganymede. Icarus 200, 207–221. https://doi.org/10.1016/j.icarus.2008.11.016.

Brummell, N.H., Hurlburt, N.E., Toomre, J., 1996. Turbulent compressible convection with rotation. I. Flow structure and evolution. Astrophys. J. 473 (1), 494–513. https://doi.org/10.1086/178161.

Chandrasekhar, S., 1961. Hydrodynamic and Hydromagnetic Stability. Oxford University Press.

Choblet, G., Tobie, G., Sotin, C., Kalousová, K., Grasset, O., 2017. Heat transport in the high-pressure ice mantle of large icy moons. Icarus 285, 252–262. https://doi.org/10.1016/j.icarus.2016.12.002.

Chyba, C.F., Phillips, C.B., 2001. Possible ecosystems and the search for life on Europa. Proc. Natl. Acad. Sci. 98, 801–804. https://doi.org/10.1073/pnas.98.3.801.

Crank, J., 1984. Free and Moving Boundary Problems. Clarendon Press.

Currie, L.K., Barker, A.J., Lithwick, Y., Browning, M.K., 2020. Convection with misaligned gravity and rotation: simulations and rotating mixing length theory. Mon. Not. R. Astron. Soc. 493 (4), 5233–5256. https://doi.org/10.1093/mnras/staa372.

Ecke, R.E., Shishkina, O., 2023. Turbulent Rotating Rayleigh–Bénard Convection. Annu. Rev. Fluid Mech. 55 (1), 603–638. https://doi.org/10.1146/annurev-fluid-120720-020446.

Gastine, T., Favier, B., 2025. Rotating convection with a melting boundary: an application to the icy moons. Icarus 429, 116441. https://doi.org/10.1016/j.icarus.2024.116441.

Goluskin, D., 2016. Internally heated convection and Rayleigh-Bénard convection. Springer International Publishing, Cham. https://doi.org/10.1007/978-3-319-23941-5.

Grötzbach, G., 1983. Spatial resolution requirements for direct numerical simulation of the Rayleigh-Bénard convection. J. Comput. Phys. 49, 241–264. https://doi.org/10.1016/0021-9991(83)90125-0.

Hussmann, H., Sotin, C., Lunine, J.I., 2015. Interiors and evolution of icy satellites. In: Treatise on Geophysics. Elsevier, pp. 605–635. https://doi.org/10.1016/B978-0-444-53802-4.00178-0.

Irion, R., 2002. Astrobiologists Try to "Follow the Water to Life". Science 1979 (296), 647–648. https://doi.org/10.1126/science.296.5568.647.

Journaux, B., Kalousová, K., Sotin, C., Tobie, G., Vance, S., Saur, J., Bollengier, O., Noack, L., Rückriemen-Bez, T., van Hoolst, T., Soderlund, K.M., Brown, J.M., 2020. Large ocean worlds with high-pressure ices. Space Sci. Rev. 216 (1), 7. https://doi.org/10.1007/s11214-019-0633-7.

Julien, K., Knobloch, E., 1998. Strongly nonlinear convection cells in a rapidly rotating fluid layer: the tilted $f$ -plane. J. Fluid Mech. 360, 141–178. https://doi.org/10.1017/S0022112097008446.

Kim, J., Moin, P., 1985. Application of a fractional-step method to incompressible Navier-stokes equations. J. Comput. Phys. 59, 308–323. https://doi.org/10.1016/0021-9991(85)90148-2.

Kunnen, R.P.J., 2021. The geostrophic regime of rapidly rotating turbulent convection. J. Turbul. 22 (4–5), 267–296. https://doi.org/10.1080/14685248.2021.1876877.

Lebec, L., Labrosse, S., Morison, A., Tackley, P.J., 2023. Scaling of convection in high-pressure ice layers of large icy moons and implications for habitability. Icarus 396, 115494. https://doi.org/10.1016/j.icarus.2023.115494.

Ledwell, J.R., Watson, A.J., Law, C.S., 1998. Mixing of a tracer in the pycnocline. J Geophys Res Oceans 103, 21499–21529. https://doi.org/10.1029/98JC01738.

Lee Allison, M., Clifford, S.M., 1987. Ice-covered water volcanism on Ganymede. J. Geophys. Res. Solid Earth 92, 7865–7876. https://doi.org/10.1029/JB092iB08p07865.

Lucchetti, A., Rossi, C., Mazzarini, F., Pajola, M., Pozzobon, R., Massironi, M., Cremonese, G., 2021. Equatorial grooves distribution on Ganymede: length and self-similar clustering analysis. Planet. Space Sci. 195, 105140. https://doi.org/10.1016/j.pss.2020.105140.

Marshall, J., Schott, F., 1999. Open-ocean convection: observations, theory, and models. Rev. Geophys. 37, 1–64. https://doi.org/10.1029/98RG02739.

Maulik, R., San, O., 2016. Dynamic modeling of the horizontal eddy viscosity coefficient for quasigeostrophic ocean circulation problems. Journal of Ocean Engineering and Science 1, 300–324. https://doi.org/10.1016/j.joes.2016.08.002.

Mitri, G., Showman, A.P., 2005. Convective–conductive transitions and sensitivity of a convecting ice shell to perturbations in heat flux and tidal-heating rate: implications for Europa. Icarus 177, 447–460. https://doi.org/10.1016/j.icarus.2005.03.019.

Moore, W., 2000. The tidal response of Europa. Icarus 147, 317–319. https://doi.org/10.1006/icar.2000.6460.

Nencioli, F., d'Ovidio, F., Doglioli, A.M., Petrenko, A.A., 2013. In situ estimates of submesoscale horizontal eddy diffusivity across an ocean front. J Geophys Res Oceans 118, 7066–7080. https://doi.org/10.1002/2013JC009252.

Nimmo, F., Pappalardo, R.T., 2016. Ocean worlds in the outer solar system. J Geophys Res Planets 121, 1378–1399. https://doi.org/10.1002/2016JE005081.

Novi, L., von Hardenberg, J., Hughes, D.W., Provenzale, A., Spiegel, E.A., 2019. Rapidly rotating Rayleigh-Bénard convection with a tilted axis. Phys. Rev. E 99 (5), 053116. https://doi.org/10.1103/PhysRevE.99.053116.

Ogura, Y., Phillips, N.A., 1962. Scale analysis of deep and shallow convection in the atmosphere. J. Atmos. Sci. 19, 173–179. https://doi.org/10.1175/1520-0469(1962)019<0173:SAODAS>2.0.CO;2.

Paluszkiewicz, T., Garwood, R., Denbo, D., 1994. Deep convective plumes in the ocean. Oceanography 7, 37–44. https://doi.org/10.5670/oceanog.1994.01.

Parodi, A., von Hardenberg, J., Passoni, G., Provenzale, A., Spiegel, E.A., 2004. Clustering of plumes in turbulent convection. Phys. Rev. Lett. 92, 194503. https://doi.org/10.1103/PhysRevLett.92.194503.

Passoni, G., Alfonsi, G., Galbiati, M., 2002. Analysis of hybrid algorithms for the Navier–Stokes equations with respect to hydrodynamic stability theory. Int. J. Numer. Methods Fluids 38 (11), 1069–1089. https://doi.org/10.1002/fld.259.

Pohorille, A., Pratt, L.R., 2012. Is water the universal solvent for life? Orig. Life Evol. Biosph. 42, 405–409. https://doi.org/10.1007/s11084-012-9301-6.

Pope, S.B., 2000. Turbulent Flows. Cambridge University Press. https://doi.org/10.1017/CBO9780511840531.

Rabbanipour Esfahani, B., Hirata, S.C., Berti, S., Calzavarini, E., 2018. Basal melting driven by turbulent thermal convection. Physical Review Fluids 3 (5), 053501. https://doi.org/10.1103/PhysRevFluids.3.053501.

Ravichandran, S., Wettlaufer, J.S., 2021. Melting driven by rotating Rayleigh–Bénard convection. J. Fluid Mech. 916, A28. https://doi.org/10.1017/jfm.2021.223.

Rayleigh, Lord, 1916. On convection currents in a horizontal layer of fluid, when the higher temperature is on the under side. The London, Edinburgh, and Dublin Philosophical Magazine and Journal of Science 32 (192), 529–546. https://doi.org/10.1080/14786441608635602.

Rovira-Navarro, M., Matsuyama, I., Berne, A., 2024. A spectral method to compute the tides of laterally heterogeneous bodies. Planet Sci J 5, 129. https://doi.org/10.3847/PSJ/ad381f.

Schubert, G., Anderson, J.D., Spohn, T., McKinnon, W.B., 2004. Interior composition, structure and dynamics of the Galilean satellites. In: Bagenal, F., Dowling, T., McKinnon, W. (Eds.), *Jupiter: The Planet, Satellites and Magnetosphere* (Capitolo 13). Cambridge University Press.

Soderlund, K., Schmidt, B., Wicht, J., et al., 2014. Ocean-driven heating of Europa's icy shell at low latitudes. Nature Geosci. 7, 16–19. https://doi.org/10.1038/ngeo2021.

Soderlund, K.M., 2019. Ocean dynamics of outer solar system satellites. Geophys. Res. Lett. 46, 8700–8710. https://doi.org/10.1029/2018GL081880.

Soderlund, K.M., Kalousová, K., Buffo, J.J., Glein, C.R., Goodman, J.C., Mitri, G., Patterson, G.W., Postberg, F., Rovira-Navarro, M., Rückriemen, T., Saur, J., Schmidt, B.E., Sotin, C., Spohn, T., Tobie, G., Van Hoolst, T., Vance, S.D., Vermeersen, B., 2020. Ice-Ocean exchange processes in the Jovian and Saturnian satellites. Space Sci. Rev. 216, 80. https://doi.org/10.1007/s11214-020-00706-6.

Spohn, T., Schubert, G., 2003. Oceans in the icy Galilean satellites of Jupiter? Icarus 161, 456–467. https://doi.org/10.1016/S0019-1035(02)00048-9.

Terra-Nova, F., Amit, H., Choblet, G., Tobie, G., Bouffard, M., Čadek, O., 2023. The influence of heterogeneous seafloor heat flux on the cooling patterns of Ganymede's and titan's subsurface oceans. Icarus 389, 115232. https://doi.org/10.1016/j.icarus.2022.115232.

Tosi, F., Mura, A., Cofano, A., Zambon, F., Glein, C.R., Ciarniello, M., Lunine, J.I., Piccioni, G., Plainaki, C., Sordini, R., Adriani, A., Bolton, S.J., Hansen, C.J., Nordheim, T.A., Moirano, A., Agostini, L., Altieri, F., Brooks, S.M., Cicchetti, A., Turrini, D., 2023. Salts and organics on Ganymede's surface observed by the JIRAM spectrometer onboard Juno. Nature Astronomy 8 (1), 82–93. https://doi.org/10.1038/s41550-023-02107-5.

van Hoolst, T., Tobie, G., Vallat, C., Altobelli, N., Bruzzone, L., Cao, H., Dirkx, D., Genova, A., Hussmann, H., Iess, L., Kimura, J., Khurana, K., Lucchetti, A., Mitri, G., Moore, W., Saur, J., Stark, A., Vorburger, A., Wieczorek, M., Witasse, O., 2024. Geophysical characterization of the interiors of Ganymede, Callisto and Europa by ESA'S JUpiter ICy moons explorer. Space Sci. Rev. 220 (5), 54. https://doi.org/10.1007/s11214-024-01085-y.

Vance, S., Bouffard, M., Choukroun, M., Sotin, C., 2014. Ganymede's internal structure including thermodynamics of magnesium sulfate oceans in contact with ice. Planet. Space Sci. 96, 62–70. https://doi.org/10.1016/j.pss.2014.03.011.

Vance, S.D., Panning, M.P., Stähler, S., Cammarano, F., Bills, B.G., Tobie, G., Kamata, S., Kedar, S., Sotin, C., Pike, W.T., Lorenz, R., Huang, H., Jackson, J.M., Banerdt, B., 2018. Geophysical investigations of habitability in ice-Covered Ocean worlds. J Geophys Res Planets 123, 180–205. https://doi.org/10.1002/2017JE005341.

Vance, S.D., Craft, K.L., Shock, E., Schmidt, B.E., Lunine, J., Hand, K.P., McKinnon, W.B., Spiers, E.M., Chivers, C., Lawrence, J.D., Wolfenbarger, N., Leonard, E.J., Robinson, K.J., Styczinski, M.J., Persaud, D.M., Steinbrügge, G., Zolotov, M.Y., Quick, L.C., Scully, J.E.C., Becker, T.M., Howell, S.M., Clark, R.N., Dombard, A.J., Glein, C.R., Mousis, O., Sephton, M.A., Castillo-Rogez, J., Nimmo, F., McEwen, A.S., Gudipati, M.S., Jun, I., Jia, X., Postberg, F., Soderlund, K.M., Elder, C.M., 2023. Investigating Europa's habitability with the Europa clipper. Space Sci. Rev. 219, 81. https://doi.org/10.1007/s11214-023-01025-2.

von Hardenberg, J., Parodi, A., Passoni, G., Provenzale, A., Spiegel, E.A., 2008. Large-scale patterns in Rayleigh–Bénard convection. Phys. Lett. A 372 (13), 2223–2229. https://doi.org/10.1016/j.physleta.2007.10.099.

Weber, J.M., Marlin, T.C., Prakash, M., Teece, B.L., Dzurilla, K., Barge, L.M., 2023. A review on hypothesized metabolic pathways on Europa and Enceladus: space-flight detection considerations. Life 13, 1726. https://doi.org/10.3390/life13081726.

Westall, F., Hickman-Lewis, K., Hinman, N., Gautret, P., Campbell, K.A., Bréhéret, J.G., Foucher, F., Hubert, A., Sorieul, S., Dass, A.V., Kee, T.P., Georgelin, T., Brack, A., 2018. A hydrothermal-sedimentary context for the origin of life. Astrobiology 18, 259–293. https://doi.org/10.1089/ast.2017.1680.

Yang, R., Howland, C.J., Liu, H.-R., Verzicco, R., Lohse, D., 2023. Morphology evolution of a melting solid layer above its melt heated from below. J. Fluid Mech. 956, A23. https://doi.org/10.1017/jfm.2023.15.

Zhu, R., Yang, H., Li, M., Chen, Z., Ma, X., Cai, J., Wu, L., 2024. Observations reveal vertical transport induced by submesoscale front. Sci. Rep. 14, 4407. https://doi.org/10.1038/s41598-024-54940-x.